ARCHIVIO ISTITUZIONALE
DELLA RICERCA

Alma Mater Studiorum Università di Bologna
Archivio istituzionale della ricerca

Limits on the nuclearite flux using the ANTARES neutrino telescope

This is the final peer-reviewed author's accepted manuscript (postprint) of the following publication:

Published Version:
A. Albert, S.A. (2023). Limits on the nuclearite flux using the ANTARES neutrino telescope. JOURNAL OF COSMOLOGY AND ASTROPARTICLE PHYSICS, 2023(1), 1-19 [10.1088/1475-7516/2023/01/012].

Availability:
This version is available at: https://hdl.handle.net/11585/940364 since: 2023-09-04

Published:
DOI: http://doi.org/10.1088/1475-7516/2023/01/012

Terms of use:

Some rights reserved. The terms and conditions for the reuse of this version of the manuscript are specified in the publishing policy. For all terms of use and more information see the publisher's website.

This item was downloaded from IRIS Università di Bologna (https://cris.unibo.it/).
When citing, please refer to the published version.

(Article begins on next page)

06 May 2026

This is the final peer-reviewed accepted manuscript of:

A. Albert et al, *Limits on the nuclearite flux using the ANTARES neutrino telescope*, JCAP01(2023)012.

The final published version is available online at: https://doi.org/10.1088/1475-7516/2023/01/012

Terms of use:

Some rights reserved. The terms and conditions for the reuse of this version of the manuscript are specified in the publishing policy. For all terms of use and more information see the publisher's website.

This item was downloaded from IRIS Università di Bologna (https://cris.unibo.it/)

When citing, please refer to the published version.

arXiv:2208.11689v5 [astro-ph.HE] 10 Dec 2022

Limits on the nuclearite flux using the ANTARES neutrino telescope

A. Albert[a,b], S. Alves[c], M. André[d], M. Ardid[e], S. Ardid[e], J.-J. Aubert[f], J. Aublin[g], B. Baret[g], S. Basa[h], B. Belhorma[i], M. Bendahman[g,j], F. Benfenati[l,m], V. Bertin[f], S. Biagi[n], M. Bissinger[o], J. Boumaaza[j], M. Bouta[p], M.C. Bouwhuis[q], H. Brânzaş[r], R. Bruijn[q,s], J. Brunner[f], J. Busto[f], B. Caiffi[t], D. Calvo[c], A. Capone[u,v], L. Caramete[r], J. Carr[f], V. Carretero[c], S. Celli[u,v], M. Chabab[w], T. N. Chau[g], R. Cherkaoui El Moursli[j], T. Chiarusi[l], M. Circella[x], J.A.B. Coelho[g], A. Coleiro[g], R. Coniglione[n], P. Coyle[f], A. Creusot[g], A. F. Díaz[y], G. de Wasseige[g], B. De Martino[f], C. Distefano[n], I. Di Palma[u,v], A. Domi[q,s], C. Donzaud[g,z], D. Dornic[f], D. Drouhin[a,b], T. Eberl[o], T. van Eeden[q], D. van Eijk[q], N. El Khayati[j], A. Enzenhöfer[f], P. Fermani[u,v], G. Ferrara[n], F. Filippini[l,m], L. Fusco[aa], J. García[e], P. Gay[ab,g], H. Glotin[ac], R. Gozzini[c], R. Gracia Ruiz[o], K. Graf[o], C. Guidi[t,ad], S. Hallmann[o], H. van Haren[ae], A.J. Heijboer[q], Y. Hello[af], J.J. Hernández-Rey[c], J. Hößl[o], J. Hofestädt[o], F. Huang[f], G. Illuminati[l,m], C. W. James[ag], B. Jisse-Jung[q], M. de Jong[q,ah], P. de Jong[q,s], M. Kadler[ai], O. Kalekin[o], U. Katz[o], A. Kouchner[g], I. Kreykenbohm[aj], V. Kulikovskiy[t], R. Lahmann[o], M. Lamoureux[g], R. Le Breton[g], D. Lefèvre[ak], E. Leonora[al], G. Levi[l,m], S. Le Stum[f], D. Lopez-Coto[am], S. Loucatos[an,g], L. Maderer[g], J. Manczak[c], M. Marcelin[h], A. Margiotta[l,m], A. Marinelli[ao], J.A. Martínez-Mora[e], K. Melis[q,s], P. Migliozzi[ao], A. Moussa[p], R. Muller[q], L. Nauta[q], S. Navas[am], E. Nezri[h], B. Ó Fearraigh[q], A. Păun[r], G.E. Păvălaş[r], C. Pellegrino[l,ap,aq], M. Perrin-Terrin[f], V. Pestel[q], P. Piattelli[n], C. Pieterse[c], C. Poirè[e], V. Popa[r], T. Pradier[a], N. Randazzo[al], D. Real[c], S. Reck[o], G. Riccobene[n], A. Romanov[t,ad], A. Sánchez-Losa[c,x], F. Salesa Greus[c], D. F. E. Samtleben[q,ah], M. Sanguineti[t,ad], P. Sapienza[n], J. Schnabel[o], J. Schumann[o], F. Schüssler[an], J. Seneca[q], M. Spurio[l,m], Th. Stolarczyk[an], M. Taiuti[t,ad], Y. Tayalati[j,k], S.J. Tingay[ag], B. Vallage[an,g], V. Van Elewyck[g,ar], F. Versari[l,m,g], S. Viola[n], D. Vivolo[ao,as], J. Wilms[aj], S. Zavatarelli[t], A. Zegarelli[u,v], J.D. Zornoza[c], J. Zúñiga[c]

(ANTARES Collaboration)

[a] *Université de Strasbourg, CNRS, IPHC UMR 7178, F-67000 Strasbourg, France*
[b] *Université de Haute Alsace, F-68100 Mulhouse, France*
[c] *IFIC - Instituto de Física Corpuscular (CSIC - Universitat de València) c/ Catedrático José Beltrán, 2 E-46980 Paterna, Valencia, Spain*
[d] *Technical University of Catalonia, Laboratory of Applied Bioacoustics, Rambla Exposició, 08800 Vilanova i la Geltrú, Barcelona, Spain*
[e] *Institut d'Investigació per a la Gestió Integrada de les Zones Costaneres (IGIC) - Universitat Politècnica de València. C/ Paranimf 1, 46730 Gandia, Spain*
[f] *Aix Marseille Univ, CNRS/IN2P3, CPPM, Marseille, France*
[g] *Université de Paris, CNRS, Astroparticule et Cosmologie, F-75013 Paris, France*
[h] *Aix Marseille Univ, CNRS, CNES, LAM, Marseille, France*
[i] *National Center for Energy Sciences and Nuclear Techniques, B.P.1382, R. P.10001 Rabat, Morocco*
[j] *Mohammed V University in Rabat, Faculty of Sciences, 4 av. Ibn Battouta, B.P. 1014, R.P. 10000 Rabat, Morocco*
[k] *Institute of Applied Physics, Mohammed VI Polytechnic University, Lot 660, Hay Moulay Rachid Ben Guerir, 43150, Morocco.*
[l] *INFN - Sezione di Bologna, Viale Berti-Pichat 6/2, 40127 Bologna, Italy*
[m] *Dipartimento di Fisica e Astronomia dell'Università, Viale Berti Pichat 6/2, 40127 Bologna, Italy*
[n] *INFN - Laboratori Nazionali del Sud (LNS), Via S. Sofia 62, 95123 Catania, Italy*
[o] *Friedrich-Alexander-Universität Erlangen-Nürnberg, Erlangen Centre for Astroparticle Physics, Erwin-Rommel-Str. 1, 91058 Erlangen, Germany*
[p] *University Mohammed I, Laboratory of Physics of Matter and Radiations, B.P.717, Oujda 6000, Morocco*
[q] *Nikhef, Science Park, Amsterdam, The Netherlands*
[r] *Institute of Space Science, RO-077125 Bucharest, Măgurele, Romania*
[s] *Universiteit van Amsterdam, Instituut voor Hoge-Energie Fysica, Science Park 105, 1098 XG Amsterdam, The Netherlands*
[t] *INFN - Sezione di Genova, Via Dodecaneso 33, 16146 Genova, Italy*

[u] INFN - Sezione di Roma, P.le Aldo Moro 2, 00185 Roma, Italy
[v] Dipartimento di Fisica dell'Università La Sapienza, P.le Aldo Moro 2, 00185 Roma, Italy
[w] LPHEA, Faculty of Science - Semlali, Cadi Ayyad University, P.O.B. 2390, Marrakech, Morocco.
[x] INFN - Sezione di Bari, Via E. Orabona 4, 70126 Bari, Italy
[y] Department of Computer Architecture and Technology/CITIC, University of Granada, 18071 Granada, Spain
[z] Université Paris-Sud, 91405 Orsay Cedex, France
[aa] Università di Salerno e INFN Gruppo Collegato di Salerno, Dipartimento di Fisica, Via Giovanni Paolo II 132, Fisciano, 84084 Italy
[ab] Laboratoire de Physique Corpusculaire, Clermont Université, Université Blaise Pascal, CNRS/IN2P3, BP 10448, F-63000 Clermont-Ferrand, France
[ac] LIS, UMR Université de Toulon, Aix Marseille Université, CNRS, 83041 Toulon, France
[ad] Dipartimento di Fisica dell'Università, Via Dodecaneso 33, 16146 Genova, Italy
[ae] Royal Netherlands Institute for Sea Research (NIOZ), Landsdiep 4, 1797 SZ 't Horntje (Texel), the Netherlands
[af] Géoazur, UCA, CNRS, IRD, Observatoire de la Côte d'Azur, Sophia Antipolis, France
[ag] International Centre for Radio Astronomy Research - Curtin University, Bentley, WA 6102, Australia
[ah] Huygens-Kamerlingh Onnes Laboratorium, Universiteit Leiden, The Netherlands
[ai] Institut für Theoretische Physik und Astrophysik, Universität Würzburg, Emil-Fischer Str. 31, 97074 Würzburg, Germany
[aj] Dr. Remeis-Sternwarte and ECAP, Friedrich-Alexander-Universität Erlangen-Nürnberg, Sternwartstr. 7, 96049 Bamberg, Germany
[ak] Mediterranean Institute of Oceanography (MIO), Aix-Marseille University, 13288, Marseille, Cedex 9, France; Université du Sud Toulon-Var, CNRS-INSU/IRD UM 110, 83957, La Garde Cedex, France
[al] INFN - Sezione di Catania, Via S. Sofia 64, 95123 Catania, Italy
[am] Dpto. de Física Teórica y del Cosmos & C.A.F.P.E., University of Granada, 18071 Granada, Spain
[an] IRFU, CEA, Université Paris-Saclay, F-91191 Gif-sur-Yvette, France
[ao] INFN - Sezione di Napoli, Via Cintia 80126 Napoli, Italy
[ap] Museo Storico della Fisica e Centro Studi e Ricerche Enrico Fermi, Piazza del Viminale 1, 00184, Roma
[aq] INFN - CNAF, Viale C. Berti Pichat 6/2, 40127, Bologna
[ar] Institut Universitaire de France, 75005 Paris, France
[as] Dipartimento di Fisica dell'Università Federico II di Napoli, Via Cintia 80126, Napoli, Italy

Abstract

In this work, a search for nuclearites of strange quark matter by using nine years of ANTARES data taken in the period 2009-2017 is presented. The passage through matter of these particles is simulated taking into account a detailed description of the detector response to nuclearites and of the data acquisition conditions. A downgoing flux of cosmic nuclearites with Galactic velocities ($\beta = 10^{-3}$) was considered for this study. The mass threshold for detecting these particles at the detector level is 4×10^{13} GeV/c^2. Upper limits on the nuclearite flux for masses up to 10^{17} GeV/c^2 at the level of $\sim 5 \times 10^{-17}$ cm^{-2} s^{-1} sr^{-1} are obtained. These are the first upper limits on nuclearites established with a neutrino telescope and the most stringent ever set for Galactic velocities.

1. Introduction

The idea of strange matter goes back to 1971 when A. Bodmer discussed collapsed nuclei [1]. In 1984 E. Witten introduced a new form of matter named strange quark matter (SQM) that could be more stable than ordinary matter [2, 3]. SQM is made up of roughly equal numbers of up, down and strange quarks with color neutrality. SQM objects are confined in a hadronic structure commonly called "bag"[4]. A bag of SQM will have a net positive charge on the surface with an almost equal electrostatic potential of + 50 MeV. This potential is adequate to repel positively charged nuclei at ordinary temperatures or at reasonably low velocities, and to attract electrons to neutralize the electric charge of SQM bags [2]. Bags can be as small as ordinary nuclei (baryon number $A \lesssim 260$) or as large as a neutron star (baryon number A $\simeq 2\times10^{57}$) [2, 5]. SQM has been studied as a part of the MIT[1] bag model for different strange quark masses and bag constants [4, 6, 7]. It could exist if it is a preferred thermodynamic phase compared to the normal state of nuclear matter consisting of protons and neutrons [8]. SQM could be formed either during the quark-hadron phase transition in the early Universe, or during the conversion of neutron stars into strange stars where strange quarks would be produced through weak processes [5, 9].

SQM produced in the early Universe was originally suggested as a candidate for dark matter [2, 7]. A. De Rújula and S. L. Glashow have discussed methods to detect the Galactic flux of SQM objects falling on Earth and used the available data to constrain the cosmic flux of SQM [10]. Usually in the literature, small ($A < 10^7$) SQM systems in the GeV-TeV range are called *strangelets*. Strangelets are outside the range of neutrino telescopes: a strangelet is searched for as an event with anomalous charge-to-mass ratio in the cosmic radiation using balloon or space-borne spectrometers. However, neutrino telescopes might detect nuclearites that penetrate at their depth. The term *nuclearites* is used to design higher mass ($A > 10^7$) objects. Nuclearites are electrically neutral atom-like systems, as they would be expected to possess an electron cloud around the core. For $A > 10^{15}$, electrons would be largely contained within the bag of nuclear matter.

Nuclearites are generally assumed to be gravitationally bound to astrophysical objects (the Galaxy, the Galaxy cluster...) and to have a speed determined by the virial theorem. In the case of nuclearites bound to the Milky Way, their velocity relative to the Solar System reference frame is $\beta \sim 10^{-3}$. Nuclearites can arrive at the Earth ground and penetrate large amounts of material, reaching underground detectors. Usually, they are searched for by cosmic ray detectors [11, 12]. These particles are protected against direct interactions with the atoms constituting the traversed medium by an electronic cloud surrounding their core. However, they would lose a large amount of energy by elastic and quasi-elastic collisions with the atoms encountered in their path. Hence, they leave a distinct signal during the passage in cosmic ray detectors. In the case of a transparent medium such as water, nuclearites signal could be detected by using the light emission from their overheated path as a black-body radiation from an expanding cylindrical thermal shock wave [10].

This work considers downgoing cosmic nuclearites arriving on the Earth with velocities $\beta = 10^{-3}$. In order to determine the threshold detection mass of these

[1] "MIT bag model" named after the institution (Massachusetts Institute of Technology) of the inventors of the model.

particles at the detector level, nuclearites with different masses are assumed to arrive vertically into the detector. The arrival speed of nuclearites at the detector depth is computed after considering their energy loss in atmosphere and sea water. Preliminary results obtained with a small ANTARES data set equivalent to 159 days of data were presented in [13].

In this paper, a brief description of the ANTARES neutrino telescope is given in section 2. Section 3 introduces the main nuclearite properties, in particular their effective cross-sectional area and the light yield in a transparent medium. The simulation of the passage of nuclearites in the ANTARES detector and the associated event selection are discussed in sections 4 and 5, respectively. The results obtained after the analysis of 9 years of data are presented and discussed in section 5.4.

2. The ANTARES neutrino telescope

ANTARES (Astronomy with a Neutrino Telescope and Abyss environmental RESearch) was a neutrino telescope based on the detection of Cherenkov radiation whose construction was completed in May 2008. The data acquisition was definitively stopped on February, 12th 2022 and the detector decommissioning ended in June 2022. It was made up of 12 vertical detection lines of 450 m length each, horizontally spaced by about $60 - 75$ m. A floor (or a storey) was formed by three optical modules (OMs) housing a 10" photomultiplier tube (PMT). A detection line was an ensemble of 25 floors spaced by 14.5 m being the first one located 100 m from the seafloor. The detector was deployed with the base of the lines at a depth of $\sim$2475 m in the Mediterranean Sea, 42 km offshore from Toulon in France. The lines were anchored to the seabed with a dead weight and were held vertical by a buoy at the top. The so-called junction box supplied the lines with electrical power and bundles the data streams from the OMs as well as the distribution of control signals to the various components. When photons of any origin impinge on the PMT photocathode, a signal can be produced at the anode and converted into a digital format by the front-end electronics boards [14], recording time and charge, and storing information in what is called a *hit*. A detailed description of the apparatus can be found in [15].

Downward going atmospheric muons and atmospheric neutrinos interacting inside or in the vicinity of the detector produce the bulk of physics signal. In fact, relativistic charged particles passing in or close to the telescope induce the production of Cherenkov photons in the medium, which can be detected by the PMTs. Nuclearites, as heavy penetrating particles, would generate visible photons from a different mechanism (described in the next section) while they penetrate into water, producing a characteristic and recognizable signal in the ANTARES detector.

3. Interaction of nuclearites with matter

Nuclearites are assumed to be heavy strange quark nuggets. For a massive nuclearite the energy loss is mainly due to the elastic and quasielastic collisions with atoms constituting the traversed medium. The energy loss per unit of length is [10]

$$-\frac{dE}{dx} = \rho\sigma v^2, \tag{1}$$

where ρ is the density of the traversed medium, v the non-relativistic velocity of the nuclearite and σ the effective cross section of the nuclearite defined as [10]

$$\sigma[\mathrm{cm}^2] = \begin{cases} \pi \times 10^{-16} & \text{if} \quad M_N < 1.5 \times 10^{-9}\ \mathrm{g} \\ \pi \times \left(\dfrac{3M_N}{4\pi\rho_N}\right)^{2/3} & \text{if} \quad M_N \geq 1.5 \times 10^{-9}\ \mathrm{g} \end{cases}, \tag{2}$$

where M_N is the nuclearite mass and $\rho_N = 3.6 \times 10^{14}$ g/cm^3 is the density of SQM objects [16]. In Eq. 2 the mass limit corresponds to a nuclearite with a radius of about 10^{-10} m. As the chemical potential of the s quark in SQM is slightly larger than for u and d quarks, finite SQM objects are always positively charged and this charge is neutralized by an electron cloud surrounding their core, thus the effective cross section for nuclearites with $M_N < 1.5 \times 10^{-9}$ g is controlled by their electronic cloud.

Nuclearites would travel with the typical velocity of gravitationally trapped objects in our Galaxy. Therefore, nuclearites are assumed entering the Earth's atmosphere with a velocity of $\beta_0 = 10^{-3}$. Before they reach the ANTARES detector they propagate through a large amount of material and interact with its constituents. For nuclearites of mass M_N penetrating a distance L in a medium of density profile $\rho(x)$, their velocity changes as [10]

$$\beta_L = \beta_0 \times \exp\left(-\frac{\sigma}{M_N}\int_0^L \rho(x)dx\right). \tag{3}$$

To simulate the propagation of nuclearites along the Earth's atmosphere, the following parametrization of its density is used [17]:

$$\rho(x) = a \times \exp\left(-\frac{x}{b}\right) = a \times \exp\left(-\frac{H - L(x)}{b}\right), \tag{4}$$

where $a = 1.2 \times 10^{-3}$ g/cm^3, $b = 8.57 \times 10^5$ cm, $H = 50$ km is the height of the atmosphere and $L(x)$ is the penetrating length in the atmosphere. For the propagation in water, a constant density of $\rho(x) = 1$ g/cm^3 is assumed.

Any experimental search for nuclearites has an acceptance of the detector for an isotropic flux of nuclearites that depends on their mass. Only nuclearites with sufficiently large mass ($> 2.5 \times 10^{22}$ GeV/c^2) can traverse the Earth at typical Galactic velocities [18]. As the flux of nuclearites should decrease when their mass increases, in this study, downward going nuclearites with masses lower than 10^{17} GeV/c^2 are considered. In fact, downward going nuclearites of larger masses are expected to cause an overall saturation of the detector, producing events with a high number of hits that could not be processed.

A summary of the detection techniques and experimental results can be found in [19, 20]. Transparent media (e.g., liquid scintillators or water) have been used in nuclearite searches. Nuclearites, as non-relativistic objects, do not produce Cherenkov light. They are expected to give rise to a thermal shock through collisions with the atoms of water. The temperature of the medium surrounding the nuclearite path rises up to the order of a few thousands of kelvin. Thus, a hot plasma is formed that moves outward as a shock wave, emitting blackbody radiation and producing many photons in the visible band. A detailed description of the luminous efficiency η defined as the fraction of dissipated energy appearing as light is given in [10]. The authors estimate that in pure water, a fraction of about 3×10^{-5} of the total energy loss is provided in form of photons in the energy range [2.25-3.75] eV.

This region is smaller than the wavelengths range in which ANTARES PMTs are sensitive (300nm-600nm). The number of visible photons radiated per unit of path length is conservatively estimated as

$$\frac{dN_\gamma}{dx} = \frac{\eta}{\pi} \times \frac{dE/dx}{\mathrm{eV}}. \tag{5}$$

The possible theoretical uncertainty on the luminous efficiency η exactly in the 300-600 nm band is within the systematic uncertainties arising from water transparency and PMT detection efficiency variation as a function of time, as discussed in sect. 6.1

At the depth of the ANTARES detector and under the previous conditions, the number I of photons reaching one photomultiplier tube is given by the integration of the number of visible photons radiated per unit of length (Eq. 5) over the nuclearite path length into the detector. The expression is given by

$$I = \int \frac{\Omega}{4\pi} \frac{dN_\gamma}{dx} \times \exp\left(\frac{-r}{\lambda_{\mathrm{att}}}\right) dx, \tag{6}$$

where Ω is the solid angle in which the optical module is seen from the emission point defined as

$$\Omega = \frac{A_{\mathrm{eff}} \times \cos(\theta)}{r^2}, \tag{7}$$

where r is the distance from the nuclearite position to the PMT and θ is the incidence angle of the photon on the PMT. The quantity λ_{att} is the light attenuation length in sea water. A_{eff} is the effective area of the PMT [15]. The number of photoelectrons in the PMT is computed including the quantum efficiency of the tubes.

4. Monte Carlo simulation

To simulate downward going nuclearites arriving at the ANTARES telescope, a hemisphere of 548 m radius has been used as a generation volume filled with water, with the value of the radius corresponding to two light attenuation lengths in water from the closest storey. The considered medium surrounds symmetrically the instrumented volume of the detector, as shown in Fig. 1. Each simulated event consists of a nuclearite generated with random position over the surface of the generation volume and with isotropic randomly generated zenith and azimuth angles (θ, φ) that define the particle direction. Since the nuclearites are assumed to arrive at the Earth with Galactic velocities, the velocity of the particle at the generation point is determined using the path crossed in sea water and atmosphere according to Eq. 3. At this stage, the particle is propagated along its direction with a time step of 2 ns. The position and the speed are evaluated at each iteration as well as the energy loss, the number of expected visible photons and the number of photoelectrons produced in each OM, which are calculated using the formulas introduced in section 3. The simulation ends when the particle exits the simulation hemisphere or when its optical energy loss (integrated over the time step) becomes too small to produce a sufficient amount of visible photons (i.e. it drops below 3 eV). At the end, the analysis tool simulates the digitization of the signal on PMTs, yielding hits as for real events.

Atmospheric muons represent the major background source for this analysis. They are produced in the decay of charged mesons generated by the interactions of primary cosmic rays with nuclei present in the atmosphere. In the simulations, they are generated in bundles and propagated down to 5 km water equivalent with the MUPAGE event generator [21]. MUPAGE is based on parametric formulas allowing to calculate the flux and angular distribution of underwater or ice muon bundles. The generator takes into account the muon multiplicity and the multi-parameter dependent energy spectrum.

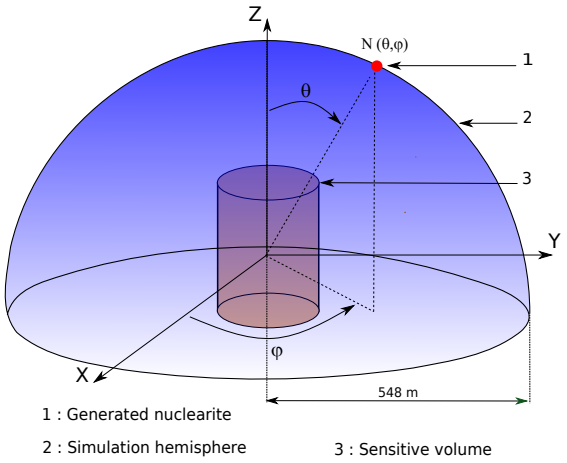

Figure 1: Simulated geometries for the event generation. Nuclearites are generated with random position over the surface of the hemisphere, isotropic randomly generated zenith and azimuth angles (θ, φ) that define the particle direction. They are propagated and only those entering in the detector sensitive volume are then considered in the simulation.

The last step of the simulation chain aims at transforming the individual light pulses into a data stream with the same format and environmental conditions as real data. In order to meet this objective, the environmental optical background due to bio-organisms and the decays of ^{40}K are added to the light produced by physics events (nuclearites or atmospheric muons). Also the behaviour of individual optical modules can be affected by local changes of environmental conditions. As a consequence, the time evolution of the data acquisition is properly reproduced, as described in [22].

5. Events selection and analysis

In order to avoid biased results, a fraction of 10% of real data has been used to define the event selection criteria and to compute the sensitivity of the detector to nuclearites. In addition, as the detection of nuclearite signals could be impacted by bioluminescence, a strict anti-bioluminescence cut is applied. A selection is made for each data taking period of several hours, which is called "run". To be considered for this analysis, a "run" should not have more than 20% of the detector elements affected by bioluminescent bursts at any moment. After applying this filter, 839 days of livetime in the period 2009-2017 are selected.

5.1. Trigger and event selection

All hits with a charge above a minimum threshold of 0.3 photoelectrons (p.e.) are denoted as L0 hits and transmitted to the shore and processed with dedicated trigger algorithms to identify potentially interesting events that are stored on disk [23]. L1 hits are defined as either a coincidence of two L0 hits in the same storey within a time window of 20 ns or a single hit with high amplitude exceeding a predefined high-threshold condition (set to 3 p.e. or 10 p.e. depending on the data acquisition conditions).

ANTARES used several trigger algorithms to filter its data. For this analysis, the standard muon triggers *T3* and *3D* are used to characterise the nuclearite signal. The 3D trigger requires at least 5 causally connected L1 hits within 2.2 μs of each other and the T3 trigger is defined as the occurrence of at least two L1 hits in three consecutive storeys within a coincidence time window. This coincidence time

window is set to 100 ns in the case that the two storeys are adjacent, and 200 ns in the case of next to adjacent storeys.

A study has been performed in order to check if low speed particles such as nuclearities are able to trigger ANTARES filters. In Fig. 2, it is presented the expected number of visible photons per centimeter, as expected from Eq. 5, as a function of the nuclearite mass. Three positions at different levels of the ANTARES detector (on the top, middle and bottom of the detector string) are considered. In that figure, nuclearites are assumed to be penetrating vertically to the detector with an initial velocity at the top of the atmosphere of $\beta_0 = 10^{-3}$. Nuclearites with a mass of 10^{13} GeV/c^2 generate less than 10^3 photons per cm. For reference, the number of Cherenkov photons in the sensitivity range of the PMTs emitted by a muon is ~ 350/cm. However, the atmospheric muon events detected by ANTARES are mostly muon bundles which emit considerably more light per cm than single muons. For example, muon bundles with multiplicity of about 80 produce about 30000 photons/cm [21], and few events of this type are expected in the considered ANTARES livetime. Therefore, a mass of 4×10^{13} GeV/c^2 is taken as a threshold mass in the analysis for nuclearite detection since it provides a light yield well separated from atmospheric events.

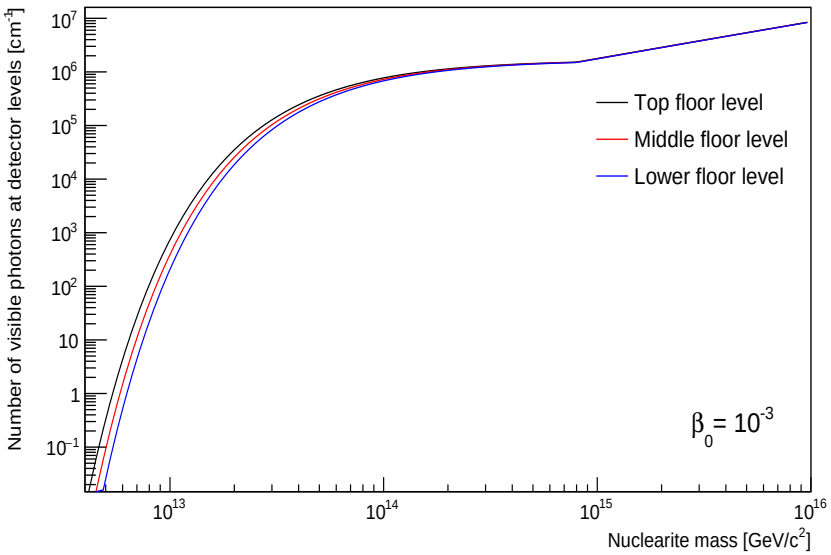

Figure 2: Number of visible [300-600 nm] photons per centimeter generated by vertically incident nuclearites at different detector levels. For masses higher than 8.4×10^{14} GeV/c^2 all electrons must be inside the quark bag. The cross section starts to increase with the nuclearite mass due to the change in the cross section, resulting in more generated visible photons.

When an event is triggered, all PMT pulses that happened within 2 μs before the first triggered hit and 2 μs after the last one are recorded. This collection of hits is referred to as a *snapshot*. In the case in which two or more events have some overlapping hits, a merging of the events is done and a larger snapshot results. As nuclearites would typically have low velocities in the detector, both T3 and 3D triggers are expected to record a series of overlapped snapshots for these particles.

The combined efficiency of ANTARES triggers depends on the nuclearite mass and its arrival direction. When averaged over an isotropic flux from the upper hemisphere, the fraction of events with mass $> 10^{14}$ GeV/c^2 recorded by the T3 or the 3D triggers ranges from 60% to almost 100% depending on the mass. The efficiency decreases for lower masses. Table 1 presents the overall efficiency for each

nuclearite mass. It is defined as the number of triggered events divided by the number of generated events. The trigger efficiency increases from 25% of generated events for nuclearites of 4×10^{13} GeV/c^2 mass to about 97% at the highest masses. The low trigger efficiency for low masses includes the effect of the energy loss of these particles from the generation surface of Fig. 1 before they reach the sensitive volume of the detector, and the fact that clipping particles are not luminous enough. These factors become negligible for high nuclearite masses.

5.2. Preliminary quality cut on L0

From the set of preselected runs, only events satisfying the predefined T3 or the 3D trigger conditions are included in this analysis. Two discriminating variables are used to isolate nuclearites signals. The first one is a dimensionless variable denoted as $\log_{10}(nhits3)/nfloor$, quantity that is proportional to the total amount of photons reaching the OMs of the detector. For a given event, $nhits3$ is the number of hits with charge of at least three photoelectrons, and $nfloor$ is the number of floors in the detector recording at least one hit for this particular event. The second discrimination variable is the event duration, dt, which represents the transit time of the event in the detector and refers to the time between the first and the last hit in the event. Nuclearites, as they are slow heavy particles, are expected to have a much larger transit time in the detector than background relativistic particles. It is important to mention that by combining these variables, the efficiency of discriminating nuclearites events increases significantly compared to usage of a single variable, as for instance the number of large intensity hits (nhits3) or the number of involved floors (nfloor).

Due to their low speed and high masses, nuclearite events would generate a high number of visible photons around the detector in a relatively long period (reaching milliseconds). They are expected to have high values for the $\log_{10}(nhits3)/nfloor$ variable as $nfloor$ is bound by the total number of detector floors. However, atmospheric muon events with low number of L0 hits affect our signal region in the $\log_{10}(nhits3)/nfloor$ variable and they must be removed. Fig. 3 illustrates $\log_{10}(nhits3)/nfloor$ versus $\log_{10}$(L0) for simulated atmospheric muon events (left) and the same quantities are presented for nuclearite with a mass of 10^{16} GeV/c^2 (right).

A first quality cut requiring at least 300 L0 hits for each event has been applied to clean our sample. This cut removes events firing with high amplitude the few PMTs present in a restricted region of the detector because of (for instance) a cascade of secondary particles induced by an atmospheric muon. Table 1 summarises the efficiency of the L0 cut for atmospheric muons and different masses of nuclearites. The efficiency is defined as the number of events after applying the L0 cut to the total number of triggered events. The L0 cut removes 85% of the simulated atmospheric muon events.

5.3. Selection efficiency

In order to discriminate nuclearite events from the background, variables that reflect the behavior of nuclearites in the detector were used. Nuclearites are expected to generate a high number of visible photons at the vicinity of the detector. This could result in a high number of fired floors with a high amplitude during a relatively long period. Fig. 4 illustrates the $\log_{10}(nhits3)/nfloor$ variable and shows the L0 cut effect on both data and atmospheric muons, for 839 days of livetime. From the right plot, most nuclearite events for different masses have a high value of this

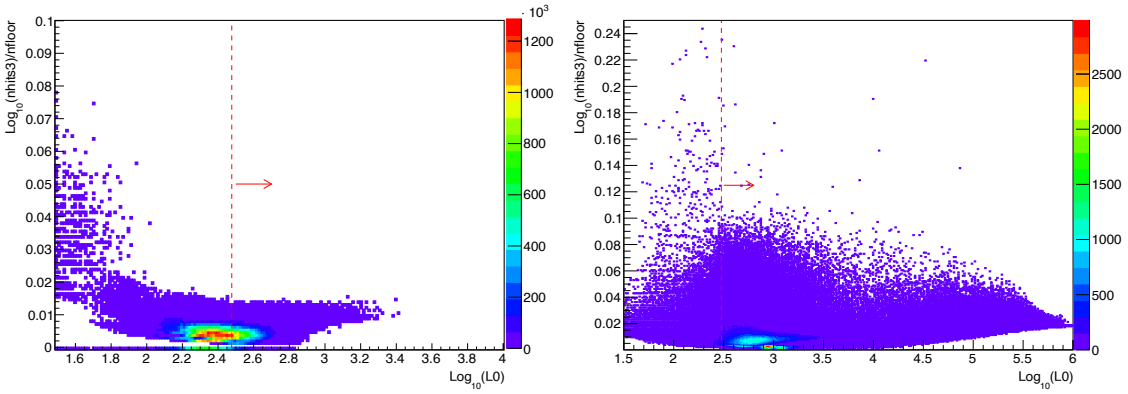

Figure 3: Distribution of $\log_{10}(nhits3)/nfloor$ versus $\log_{10}$(L0) for simulated atmospheric muons (left), and for nuclearites with a mass of 10^{16} GeV/c^2 (right). The palette of colors for the left panel represents the expected number of events in 839 days of livetime, while for the right panel represents the number of simulated events. The cut at 300 L0 hits (red dashed line) allows to reject background events with high values of $\log_{10}(nhits3)/nfloor$ characterized by a low number of L0 hits. Only 16% of the simulated atmospheric muons survive the L0 cut.

variable compared to muon events whose distribution stop at around ∼0.015. The signal of these particles is also characterised by a long snapshot duration.

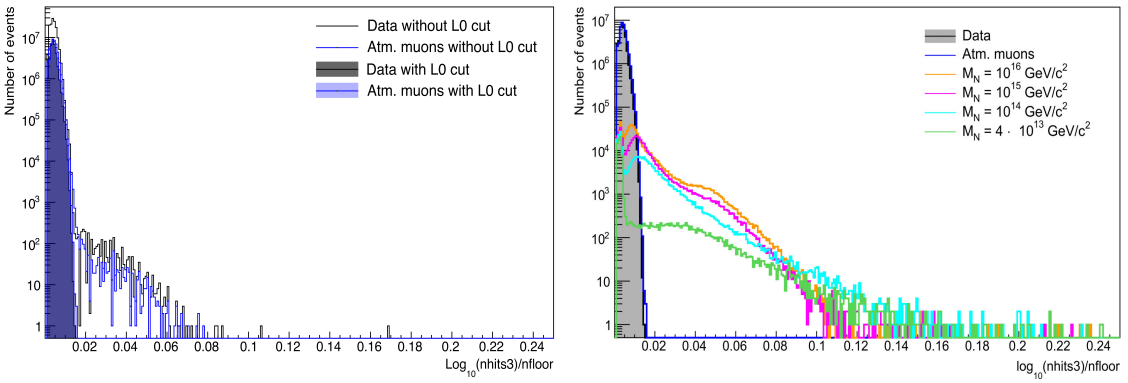

Figure 4: Left: Distribution of the discrimination variable $\log_{10}(nhits3)/nfloor$ without and with the cut L0 $\geq$ 300 on the total number of PMT hits using 839 days of livetime. The black histogram corresponds to data, while the blue one refers to simulated atmospheric muons. Right: The same distribution with the L0 $\geq$ 300 cut for data, simulated atmospheric muons and simulated and triggered nuclearites with different masses (other colors).

In order to reduce the background, events are selected based on both parameters characterizing the signal. Fig. 5 shows $\log_{10}(nhits3)/nfloor$ versus dt for each nuclearite mass. An important fraction of nuclearite events show a long duration, dt, typically higher than 3×10^3 ns, combined with high values of $\log_{10}(nhits3)/nfloor$. The scatter plots in Fig. 5 show that both variables are well suited to discriminate between nuclearites and background from cosmic ray muons. By applying the appropriate cuts, the region dominated by the noise could easily be discriminated from the region relevant for our signal. However, in order to maximise the performance of these cuts, an optimisation is required. The methods used to optimise the cuts are discussed in the next subsection. As a result, the signal to background discrimination is maximized by removing events according to the conditions:

$$\log_{10}(dt/1\text{ns}) < 4.125 \; .AND. \; \log_{10}(nhits3)/nfloor < 0.025 \qquad (8)$$

Table 1 shows the selection efficiency of the optimised cuts for each nuclearite mass.

Nuclearite mass (GeV/c^2)	10^{16}	10^{15}	10^{14}	4×10^{13}	Atm. muons
Trigger efficiency (%)	97	88	61	25	9.5
L0 cut efficiency (%)	40	42	31	17	15
Selection efficiency (%)	18	19	25	68	0
Final efficiency (%)	6.9	7.0	4.7	2.8	0

Table 1: Selection efficiencies as a function of the nuclearite masses at the different steps discussed in the text. The trigger efficiency in the first row is computed with respect to the number of simulated events, while the efficiencies in the following rows are computed with respect to the previous one. The selection efficiency of atmospheric muons are also reported in the last column.

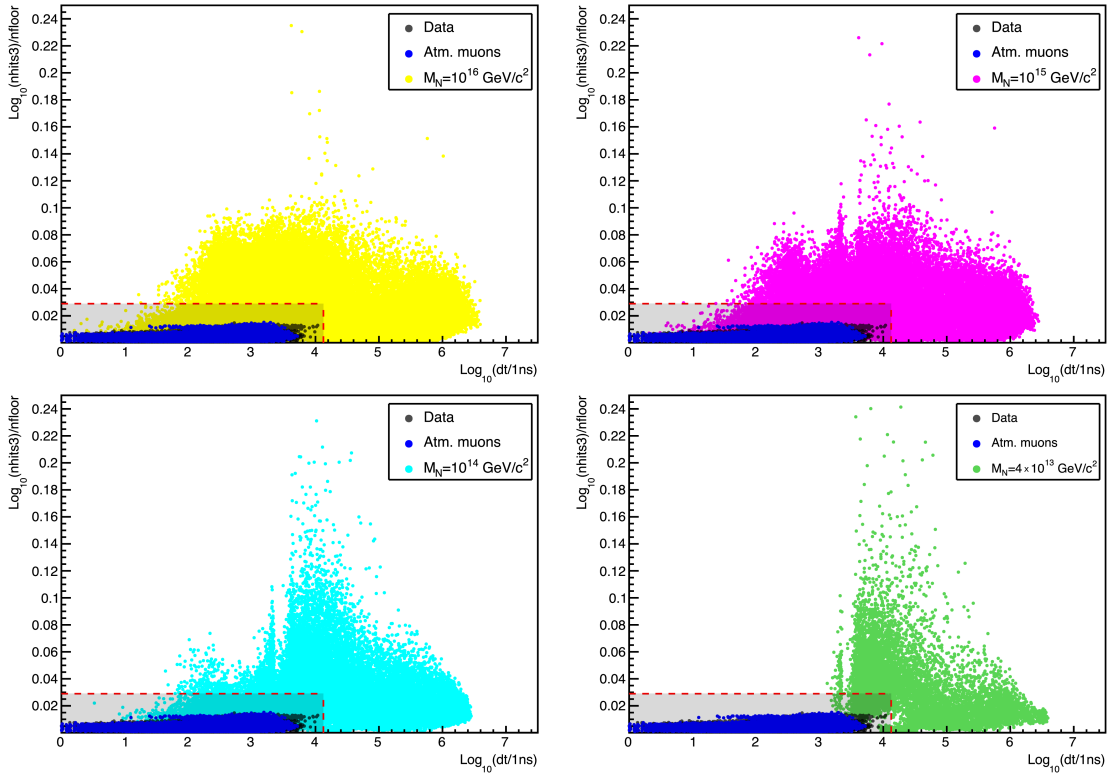

Figure 5: Scatter plot of $\log_{10}(nhits3)/nfloor$ versus $\log_{10}(dt/1\text{ns})$ for events with at least 300 L0 hits. Real data in black, atmospheric muons in blue, and for different nuclearite masses. The red dotted lines represent the optimised cuts on both discrimination variables.

5.4. Optimization of the two variables

In order to achieve the best sensitivity of ANTARES to nuclearites without any bias, the Model Rejection Factor (MRF) is used [24] to optimise the cuts on the discrimination variables taking into account the statistical fluctuations in the simulated atmospheric muons distributions. The MRF technique consists of varying the cuts with small steps until the minimum of MRF is reached, this minimum corresponds to the values that give the best sensitivity.

The sensitivity at 90% confidence level (CL), denoted as S_{90}, is computed using the Feldman-Cousins method [25], assuming events with a Poissonian distribution:

$$\bar{\mu}_{90} = \sum_{n_{\rm obs}=0}^{\infty} \mu_{90}(n_{\rm obs}, n_{\rm b}) \times \frac{n_{\rm b}^{n_{\rm obs}}}{n_{\rm obs}!} \times e^{-n_{\rm b}}, \tag{9}$$

$$S_{\rm eff} = \frac{n_{\rm Nuc}}{\Phi_{\rm Nuc}}, \tag{10}$$

$$S_{90} = \frac{\bar{\mu}_{90}(n_{\rm b})}{S_{\rm eff} \times T}, \tag{11}$$

where $n_{\rm obs}$ is the number of observed events and $n_{\rm b}$ the number of expected background events from the full dataset. T is the duration of data taking corresponding to the 2009-2017 period and $\mu_{90}(n_{\rm obs}, n_{\rm b})$ represents the upper limit for $n_{\rm obs}$ events and $n_{\rm b}$ expected backgroung events. $n_{\rm Nuc}$ denotes the number of nuclearites remaining after applying the optimized cuts, and $\Phi_{\rm Nuc}$ the corresponding flux of generated nuclearites.

The best values on dt and $\log_{10}(nhits3)/nfloor$ are those minimising the MRF for each nuclearite mass. Fig. 6 shows an example of the MRF for the highest nuclearite mass as a function of the selection parameters. The values that minimise the MRF for the four values of the simulated nuclearite masses are reported in the first two rows of Table 2. The fraction of event passing all the selection criteria is reported in the third row, while the number of remaining background events after the selection cuts and the value of the MRF are in the rows 4 and 5, respectively.

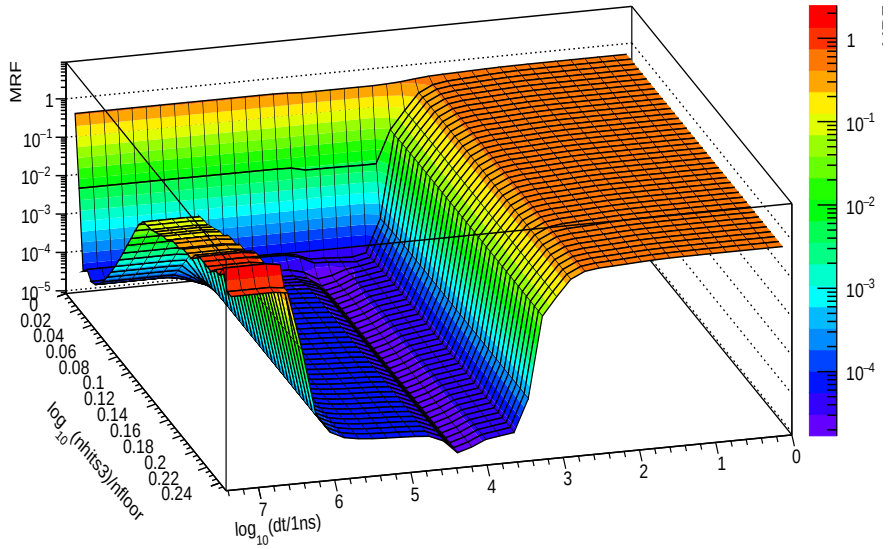

Figure 6: MRF as function of $\log_{10}(nhits3)/nfloor$ and dt for the highest nuclearite mass considered (10^{16} GeV/c^2).

6. Systematic effects and experimental results

6.1. Systematic uncertainties

Experimental searches of nuclearites rely on the crossing time of the particles in the detector and the light yield per unit length of the track, as given in the De Rújula and Glashow paper [10]. Following [10], in the present paper the luminous efficiency η as derived for transparent water in the [550-330] nm wavelength range was used. This wavelength region is well within sensitivity of ANTARES PMTs. The energy distribution of photons follows the black-body distribution, which for nuclearites

Nuclearite mass (GeV/c^2)	10^{16}	10^{15}	10^{14}	4×10^{13}
Best cut on $\log_{10}(dt/1\text{ns})$	≥ 4.27	≥ 4.27	≥ 4.27	≥ 4.35
Best cut on $\log_{10}(nhits3)/nfloor$	≥ 0.029	≥ 0.024	≥ 0.024	≥ 0.024
Remaining nuclearites (%)	6.9	7.0	4.7	2.8
Remaining background	1.05	0.35	0.35	0.31
MRF	1.6×10^{-5}	2×10^{-5}	2.7×10^{-5}	4.12×10^{-5}
Flux upper limit 90 %CL (cm$^{-2}\times$ sr$^{-1}\times$ s^{-1})	6.6×10^{-18}	8.1×10^{-17}	1.1×10^{-17}	1.6×10^{-17}

Table 2: Values of the optimised parameters and the results of the MRF and upper limits for the different nuclearite masses for 839 days of livetime.

arriving in the detector with masses above the threshold of 4×10^{13} GeV/c^2 has a peak at wavelengths shorted than 300 nm. The intensity of Cherenkov emission produced by relativistic particles is proportional to $1/\lambda^2$, and also in this case short wavelengths dominate. When the two different spectra are folded in our simulations with the water transmission [27] and the quantum efficiency the PMTs as a function of the wavelength [26], the differences between the two different spectra in the photoelectron yields on the PMTs are within 30-40%. The minimum nuclearite mass (4×10^{13} GeV/c^2) considered in the analysis ensures that the number of emitted photons per cm are of the order of 10^6 at each detector depth: as a consequence, the trigger and selection efficiencies are not affected by the variation in the emission spectra of visible photons.

The uncertainties for the signal produced by atmospheric muons are derived from the statistical fluctuations in the signal region for both discrimination variables (dt and $\log_{10}(nhits3)/nfloor$); this is recovered by extrapolating the distributions using a Landau type function (see ref. [28] for further details). Systematic uncertainties on the effect of atmospheric muon events are mainly due to the detector description and to the knowledge on the environmental parameters. These are mainly related to the uncertainties on the angular acceptance of the optical modules and on the light absorption and scattering lengths in the sea water [26, 27]. Hence, an overall of +35% -30% effect on the expected atmospheric muon rate results from ±15% as a maximum of uncertainty on the optical module acceptance and ±10% on the light absorption in water along the entire wavelength spectrum [29]. The computation of the number of observed events n_{obs} and the number of expected background events n_b given in equation 9 incorporate systematic uncertainties using the method described in [30].

6.2. Unblinding results

After unblinding the remaining 90% of data not used for testing the optimisation procedure, no event is present in the region beyond the optimised cuts. Since no event is found, the upper limit on the flux of nuclearites at 90% CL is computed as

$$\phi_{90} = \frac{\mu_{90}(n_{\rm obs}, n_{\rm b})}{S_{\rm eff} \times T}, \tag{12}$$

where the confidence interval at 90% CL $\mu_{90}(n_{\rm obs}, n_{\rm b})$ is computed from the unified approach of Feldman-Cousins [25]. S_{eff} is defined in equation 10 and T is the livetime of the analysis.

The 90% CL flux upper limit values reported in Table 2 include both statistical and systematic uncertainties.

The obtained upper limit (UL) on the nuclearite flux for $T = 839$ days of livetime of the ANTARES detector is shown in Fig. 7. For masses higher than 10^{16} GeV/c^2,

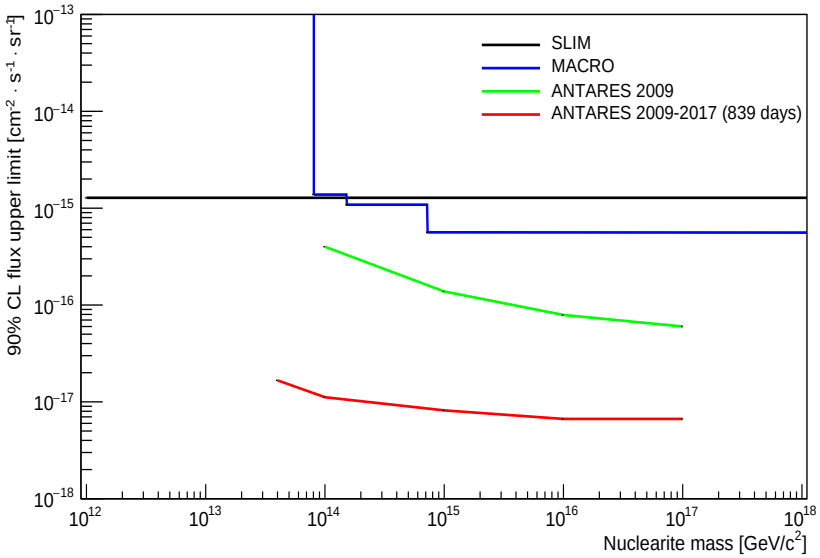

Figure 7: Upper limit on the flux of nuclearites with Galactic velocities ($\beta = 10^{-3}$) in red line, using 839 days of livetime in the period 2009-2017 with the ANTARES detector. The green line corresponds to a previous ANTARES result obtained with a smaller data sample [13]. Results from other experiments, MACRO [19] and SLIM [20], are also shown.

nuclearites emit more light. Therefore, the limit of the last test point can be taken as a conservative limit also for higher nuclearite masses, up to the value of $\sim 10^{17}$ GeV/c^2 where detector saturation effects start to occur.

7. Conclusion

A search for nuclearites in the mass range from 4×10^{13} GeV/c^2 to 10^{16} GeV/c^2 reaching the ANTARES neutrino telescope using nine years of data (for an equivalent livetime of 839 days) is presented. Typical Galactic velocities ($\beta = 10^{-3}$) at the surface of the Earth atmosphere have been considered for this study. After propagation down to the sea level, a large fraction of events trigger the apparatus and they are discriminated against the background formed by atmospheric muon bundles. The selection efficiency increases with increasing nuclearite masses. No events survive the selection cuts and 90% CL upper limits are derived as a function of the nuclearite mass. These are the most stringent limits ever set for nuclearites with Galactic velocities and the first ones set by a neutrino telescope.

Acknowledgments

The authors acknowledge the financial support of the funding agencies: Centre National de la Recherche Scientifique (CNRS), Commissariat à l'énergie atomique et aux énergies alternatives (CEA), Commission Européenne (FEDER fund and Marie Curie Program), Institut Universitaire de France (IUF), LabEx UnivEarthS (ANR-10-LABX-0023 and ANR-18-IDEX-0001), Région Île-de-France (DIM-ACAV), Région Alsace (contrat CPER), Région Provence-Alpes-Côte d'Azur, Département du Var and Ville de La Seyne-sur-Mer, France; Bundesministerium für Bildung und Forschung (BMBF), Germany; Istituto Nazionale di Fisica Nucleare (INFN), Italy; Nederlandse organisatie voor Wetenschappelijk Onderzoek (NWO), the Netherlands; Executive Unit for Financing Higher Education, Research, Development and Innovation (UEFISCDI), Romania; Ministerio de Ciencia, Innovación, Investigación y

Universidades (MCIU): Programa Estatal de Generación de Conocimiento (refs. PGC2018-096663-B-C41, -A-C42, -B-C43, -B-C44 and refs. PID2021-124591NB-C41, -C42, -C43) (MCIU/FEDER), Generalitat Valenciana: Prometeo (PROMETEO/2020/019), Grisolía (refs. GRISOLIA/2018/119, /2021/192) and GenT (refs. CIDEGENT/2018/034, /2019/043, /2020/049, /2021/023) programs, Junta de Andalucía (ref. A-FQM-053-UGR18), La Caixa Foundation (ref. LCF/BQ/IN17/11620019), EU: MSC program (ref. 101025085), Spain; Ministry of Higher Education, Scientific Research and Innovation, Morocco, and the Arab Fund for Economic and Social Development, Kuwait. We also acknowledge the technical support of Ifremer, AIM and Foselev Marine for the sea operation and the CC-IN2P3 for the computing facilities.

References

[1] A. Bodmer, *Collapsed Nuclei*, Phys. Rev. D 4 (1971) 1601.

[2] E. Witten, *Cosmic separation of phases*, Phys. Rev. D 30 (1984) 272-285.

[3] H. Terazawa, *Super-Hypernuclei in the Quark-Shell Model. II* , J. Phys. Soc. Japan, 58 (1989), 4388-4393.

[4] E. Farhi and R. L. Jaffe, *Strange matter*, Phys. Rev. D 30 (1984), 2379.

[5] A. Bauswein, H.-T. Janka, R. Oechslin, G. Pagliara, I. Sagert, J. Schaffner-Bielich, M. M. Hohle, and R. Neuhäuser, *Mass Ejection by Strange Star Mergers and Observational Implications*, Phys. Rev. Lett. 103 (2009), 011101.

[6] A. Chodos, R. L. Jaffe, K. Johnson, and C. B. Thorn, *Baryon structure in the bag theory*, Phys. Rev. D 10 (1974), 2599.

[7] T. DeGrand, R. L. Jaffe, K. Johnson, and J. Kiskis, *Masses and other parameters of the light hadrons*, Phys. Rev. D 12 (1975), 2060.

[8] C. Greiner, A. Diener, J. Schaffner, H. Stoecker, *Strange matter — a new domain of nuclear physics*, Nucl. Phys. A 566 (1994), 157-165.

[9] J. D. Bjorken and L. D. McLerran, *Explosive quark matter and the "Centauro" event*, Phys. Rev. D 20 (1979), 2353.

[10] A. De Rújula and S. L. Glashow, *Nuclearites - a novel form of cosmic radiation*, Nature 312 (1984), 734–737.

[11] J. Madsen, *Strangelet propagation and cosmic ray flux*, Phys. Rev. D 71 (2005), 014026.

[12] M. Spurio, *Searches for Magnetic Monopoles and other Stable Massive Particles*, arXiv: 1906.02039 [hep-ph].

[13] G. E. Păvălaş [ANTARES Collaboration], *Search for nuclearites with the ANTARES neutrino telescope*, Proceedings of The 34th International Cosmic Ray Conference — PoS(ICRC2015), 236 (2015), 1060.

[14] J. A. Aguilar [ANTARES Collaboration], *Performance of the front-end electronics of the ANTARES neutrino telescope*, Nucl. Instrum. Meth. A 622 (2010) 59 [arXiv:1007.2549].

[15] M. Ageron [ANTARES Collaboration], *ANTARES: the first undersea neutrino telescope*, Nucl. Instrum. Meth. A 656 (2011), Issue 1, 11-38.

[16] S. A. Chin and A. K. Kerman, *Possible Long-Lived Hyperstrange Multiquark Droplets*, Phys. Rev. Lett. 43, 1292.

[17] T. Shibata, *Study of Shower Phenomena in the Atmosphere. I: Analytical Derivation of Lateral Structure Function of Hadronic Components*, Prog. Theor. Phys. 57 (1977), Issue 3, 882–900.

[18] Wan-Lei Guo, Cheng-Jun Xia, Tao Lin, and Zhi-Min Wang, *Exploring detection of nuclearites in a large liquid scintillator neutrino detector*, Phys. Rev. D 95 (2017), 015010.

[19] M. Ambrosio [MACRO Collaboration], *Nuclearite search with the MACRO detector at Gran Sasso*, Eur. Phys. J. C 13 (2000), 453–458 .

[20] S. Balestra et al, *Results of the search for strange quark matter and Qballs with the SLIM experiment*, Eur. Phys. Jour. C 57 (2008), 525.

[21] G. Carminati, M. Bazzotti, A. Margiotta and M. Spurio, *Atmospheric MUons from PArametric formulas: a fast GEnerator for neutrino telescopes (MUPAGE)*, Comput. Phys. Commun. 179 (2008), Issue 12, 915-923.

[22] A. Albert [ANTARES Collaboration], *Monte Carlo simulations for the ANTARES underwater neutrino telescope*, J. Cosmol. Astropart. Phys. (2021).

[23] J. A. Aguilar [ANTARES Collaboration], *The data acquisition system for the ANTARES Neutrino Telescope*, Nucl. Instrum. Meth. A 570 (2007) 107 [astro-ph/0610029].

[24] G. C. Hill and K. Rawlins, *Unbiased cut selection for optimal upper limits in neutrino detectors: the model rejection potential technique*, Astropart. Phys. 19 (2003), Issue 3, 393-402.

[25] Gary J. Feldman and Robert D. Cousins, *Unified approach to the classical statistical analysis of small signals*, Phys. Rev. D 57 (1998), 3873 .

[26] P. Amram [ANATRES Collaboration], *The ANTARES optical module*, Nucl. Instrum. Methods Phys. Res. A: Accel. Spectrom. Detect. Assoc. Equip. 484 (2002), 1–3, 369-383.

[27] J. A. Aguilar [ANTARES Collaboration], *Transmission of light in deep sea water at the site of the ANTARES*, Astropart. Phys. 23 (2005) 131-155.

[28] A. Albert et al. (ANTARES Collaboration), *Search for magnetic monopoles with ten years of the ANTARES neutrino telescope*, JHEAp 34 (2022) 1-8.

[29] J. A. Aguilar [ANTARES Collaboration], *Zenith distribution and flux of atmospheric muons measured with the 5-line ANTARES detector*, Astropart. Phys. 34 (2010) 179-184.

[30] J. Conrad, O. Botner, A. Hallgren, and C. Pérez de los Heros *Including systematic uncertainties in confidence interval construction for Poisson statistics*, Phys. Rev. D 67, 012002 (2003).